



Strato-mesospheric ClO observations by SMILES: error analysis and diurnal variation

T. O. Sato^{1,2}, H. Sagawa², D. Kreyling², T. Manabe³, S. Ochiai², K. Kikuchi², P. Baron², J. Mendrok^{4,2}, J. Urban⁵,
D. Murtagh⁵, M. Yasui², and Y. Kasai^{2,1}

¹Tokyo Institute of Technology, 4259 Nagatsuta-cho, Midori-ku, Yokohama, Kanagawa 226-8503, Japan

²National Institute of Information and Communications Technology, 4-2-1 Nukui-kitamachi, Koganei, Tokyo 184-8795, Japan

³Osaka Prefecture University, 1-1 Gakuen-cho, Naka-ku, Sakai, Osaka 599-8531, Japan

⁴Luleå University of Technology, P.O. Box 812, 98128 Kiruna, Sweden

⁵Chalmers University of Technology, Department of Earth and Space Sciences, 41296 Gothenburg, Sweden

Correspondence to: T. O. Sato (sato.t.ak@m.titech.ac.jp)

Received: 24 May 2012 – Published in Atmos. Meas. Tech. Discuss.: 4 July 2012

Revised: 18 October 2012 – Accepted: 19 October 2012 – Published: 20 November 2012

Abstract. Chlorine monoxide (ClO) is the key species for anthropogenic ozone losses in the middle atmosphere. We observed ClO diurnal variations using the Superconducting Submillimeter-Wave Limb-Emission Sounder (SMILES) on the International Space Station, which has a non-sun-synchronous orbit. This includes the first global observations of the ClO diurnal variation from the stratosphere up to the mesosphere. The observation of mesospheric ClO was possible due to 10–20 times better signal-to-noise (S/N) ratio of the spectra than those of past or ongoing microwave/submillimeter-wave limb-emission sounders. We performed a quantitative error analysis for the strato- and mesospheric ClO from the Level-2 research (L2r) product version 2.1.5 taking into account all possible contributions of errors, i.e. errors due to spectrum noise, smoothing, and uncertainties in radiative transfer model and instrument functions. The SMILES L2r v2.1.5 ClO data are useful over the range from 0.01 and 100 hPa with a total error estimate of 10–30 pptv (about 10 %) with averaging 100 profiles. The SMILES ClO vertical resolution is 3–5 km and 5–8 km for the stratosphere and mesosphere, respectively. The SMILES observations reproduced the diurnal variation of stratospheric ClO, with peak values at mid-day, observed previously by the Microwave Limb Sounder on the Upper Atmosphere Research Satellite (UARS/MLS). Mesospheric ClO demonstrated an opposite diurnal behavior, with nighttime values being larger than daytime values. A

ClO enhancement of about 100 pptv was observed at 0.02 to 0.01 hPa (about 70–80 km) for 50° N–65° N from January–February 2010. The performance of SMILES ClO observations opens up new opportunities to investigate ClO up to the mesopause.

1 Introduction

Chlorine monoxide (ClO) is a primary form of reactive chlorine and a key intermediate for ozone losses. The partitioning of the reactive and reservoir forms of the halogen species modulates the destruction of ozone. Chemical ozone losses are mostly controlled by spatio-temporal distributions of active halogens. For example, ClO activation on surfaces of polar stratospheric cloud due to low temperatures produced the strong Arctic ozone depletion during the winter of 2010/2011 (Manney et al., 2011). Microwave spectroscopic remote sensing from space is one of the best methods of obtaining global ClO distributions in the Earth's middle atmosphere. There have been four satellite instruments so far that enable the ClO global distributions to be observed. The first satellite observation of ClO was accomplished by the Microwave Limb Sounder (MLS) on board the Upper Atmosphere Research Satellite (UARS), which was launched by NASA in 1991 (Waters et al., 1993); the UARS/MLS measured the ClO transition at 204.4 GHz. The Sub-Millimetre

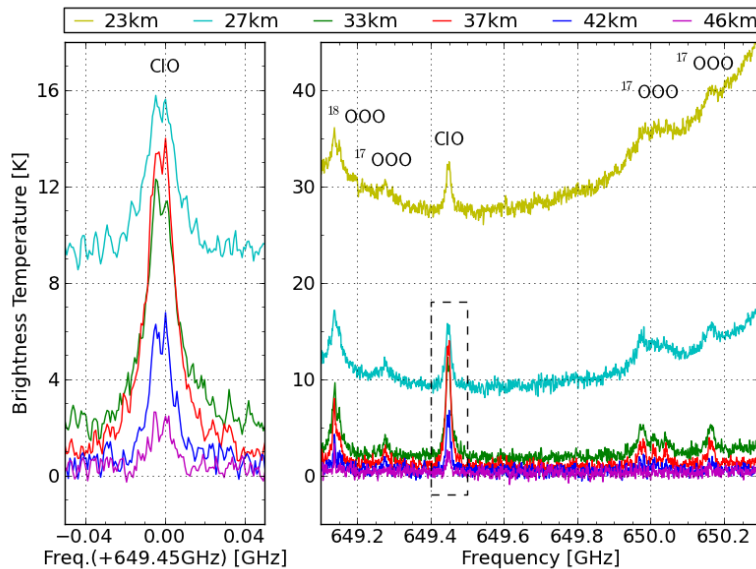


Fig. 1. Single-scan Band C spectra observed by SMILES at tangent heights of 23, 27, 33, 37, 42 and 46 km. The frequency is calibrated by considering Doppler shift. The figure at left is a magnification of the ClO transitions at 649.445 and 649.451 GHz. The figure at right shows the full frequency region for Band C. Date: 9 November 2009. LT (local time): 00:22. Latitude: 57.2° N. Longitude: 6.4° E.

Radiometer on board the Odin satellite (Odin/SMR) was launched in February 2001 and has been observing ClO using the transition at 501.3 GHz (Murtagh et al., 2002). Aura/MLS was launched in 2004 and has been observing ClO using the transition at 649.4 GHz (Waters et al., 2006). The Superconducting Submillimeter-Wave Limb-Emission Sounder (SMILES) also observed ClO using the same transition as Aura/MLS but with much more sensitive technology. SMILES made observations from the Japanese Experiment Module (JEM) of the International Space Station (ISS) between 12 October 2009 and 21 April 2010 (Kikuchi et al., 2010).

The SMILES observations were notable in that they were (1) the first passive observations of the Earth's atmosphere with a sensitive 4-K submillimeter-wave receiver and (2) the most sensitive observations of short-lived atmospheric species with diurnal variations, which were achieved by the non-sun-synchronous orbit of the ISS.

The SMILES instrument employs superconductor-insulator-superconductor (SIS) mixers cooled at about 4 K and high-electron-mobility-transistor (HEMT) amplifiers at 20 and 100 K. The receiver system achieves a low system noise temperature (T_{sys}) of about 350 K and a signal-to-noise (S/N) ratio of about 50 for stratospheric ClO at mid-latitudes for a single-scan spectrum. T_{sys} achieved with receiver systems using conventional Schottky diodes is about 3000–6000 K in the 500–600 GHz region for passive satellite observations. The SMILES target species are O₃, ClO, H³⁵Cl, H³⁷Cl, O₃ isotopomers, BrO, HO₂, HOCl, CH₃CN and HNO₃ in the stratosphere and the mesosphere, as well as H₂O and ice clouds in the upper troposphere/lower

stratosphere. SMILES has three observation frequency bands of Band A (624.32–625.52 GHz), Band B (625.12–626.32 GHz) and Band C (649.12–650.32 GHz). The ClO transitions observed by using SMILES in the ground rovibronic state (Λ -type doubling, $J = 35/2-33/2$) are located at 649.445 and 649.451 GHz in Band C (Fig. 1). Two of the three frequency bands were used simultaneously, as in simultaneous observations using Bands A and B, Bands B and C, or Bands C and A, since SMILES had two spectrometers. About 70 % of all observations were for Band C. SMILES observed the Earth's limb from the JEM/ISS at an altitude of 330–370 km. The latitudes covered by SMILES observations were normally 38° S–65° N. About 1600 points were observed daily by SMILES. The SMILES antenna limb scans were normally performed from 0 to 100 km.

We quantitatively evaluated a total error in the ClO observations taking into account all known contributions of errors, i.e. errors due to spectrum noise, smoothing, and uncertainties in radiative transfer model and instrument functions. An error due to inaccuracy in spectrum calibration was also evaluated. Uncertainties of the error contributions were conservatively determined based on the laboratory and in-orbit measurements made by the SMILES mission team for the Level-2 research (L2r) product version 2.1.5. Section 2 describes all error sources considered in this study and methods of calculating the errors in the SMILES ClO observations. In Sect. 3, we described results of the error analysis. Section 4 described diurnal variations observed by SMILES. Stratospheric ClO diurnal variations observed by SMILES were compared to those observed by UARS/MLS. Diurnal

variations of the mesospheric ClO up to 80 km were observed by SMILES for the first time from space.

The retrieval algorithm of the L2r version 2.1.5 was optimized for the middle stratosphere up to the mesosphere. We focused on ClO in the middle stratosphere and the mesosphere at equator and mid-latitude regions. A polar enhanced ClO at lower stratosphere was not discussed in this paper. Several issues for retrieval in the lower stratosphere are planned to be improved in the next version of L2r product.

2 Method of characterizing error

We have performed an error analysis for volume mixing ratio (VMR) profile of ClO using a single-scan spectrum. The error in the ClO profile resulted from spectrum statistics noise and also from inaccuracy in spectrum synthesis using forward model and spectrum calibration.

2.1 Uncertainties in synthesized and observed spectra

2.1.1 Calculation of radiative transfer

We used the Advanced Model for Atmospheric Terahertz Radiation Analysis and Simulation (AMATERASU) (Baron et al., 2008) for clear-sky radiative transfer calculations and instrument functions, which was also used for calculation of the L2r version 2.1.5 (Baron et al., 2011). The details on the forward model calculations are described by Urban et al. (2004). Radiance intensity at frequency ν is calculated using a total absorption coefficient k_ν :

$$k_\nu(s) = \sum_{p,q} \rho^p(s) J_{\nu_q}^q(T) \frac{\nu}{\nu_q} f_\nu(\nu_q, w_q) + k_\nu^{\text{cont}}(s), \quad (1)$$

where s is the line-of-sight, $\rho^p(s)$ is the number density of the species p , ν_q is the frequency of the transition q , $J_{\nu_q}^q(T)$ is the line intensity of the transition q at the temperature T , $f_\nu(\nu_q, w_q)$ is the line shape function for the transition q , w_q is the line width of the transition q and $k_\nu^{\text{cont}}(s)$ is the continuum absorption coefficient. Line width w consists of collisional broadening width w_{col} , and Doppler broadening width w_{dop} . w_{col} is described using air-broadening coefficient γ_{air} as

$$w_{\text{col}} = \gamma_{\text{air}}(T) P (1 - x_{\text{VMR}}) + \gamma_{\text{self}}(T) P x_{\text{VMR}}, \quad (2)$$

where P is the pressure, x_{VMR} is the VMR and γ_{self} is the self-broadening coefficient. The self-broadening effects for ClO are much smaller than the air-broadening effects since x_{VMR} is much smaller than 1 (the VMR of ClO is of order 10^{-9}). Equation (2) therefore reduces to $\gamma_{\text{air}}(T) P$. γ_{air} depends on the temperature T with a factor n_{air} written as

$$\gamma_{\text{air}}(T) = \gamma_{\text{air}}(T_0) \left(\frac{T}{T_0} \right)^{-n_{\text{air}}} \quad (T_0 = 296 \text{ K}). \quad (3)$$

Line-by-line calculations were performed using a dedicated spectroscopic database for SMILES observations. The lines included in the SMILES spectroscopic database were selected according to the line selection algorithm (Sato, 2010; Baron et al., 2011) from the lines listed in the JPL spectroscopic catalog (Pickett et al., 1998) and the HITRAN 2008 catalog (Rothman et al., 2009). There were about 1200 lines in the SMILES spectroscopic database. The line intensities and the transition frequencies were adopted from the JPL catalog with some replacements with recent laboratory measurements (Cazzoli and Puzzarini, 2004, H. Ozeki, personal communication, 2010; W. G. Read, personal communication, 2011). The air-broadening coefficients, γ_{air} and n_{air} , were taken from the HITRAN 2008 catalog and the laboratory measurements (Drouin and Gamache, 2008; Hoshina et al., 2008; Sato et al., 2010; Drouin, 2007; Markov and Krupnov, 1995; Mizoguchi et al., 2012; Perrin et al., 2005, e.g. W. G. Read, personal communication, 2011). The ClO spectroscopic parameters relevant to the SMILES observations are given in Table 1. The Van Vleck and Weisskopf profile (van Vleck and Weisskopf, 1945) was used as the line shape function at the lower altitudes where the Doppler broadening width was less than 1/40th of the collisional broadening width, and the Voigt profile (Schreier and Kohlert, 2008) was used at the higher altitudes. Continuum absorption coefficients of humid and dry air were based on atmospheric opacity measurements made by Pardo et al. (2001). The dry-air continuum model was multiplied by 1.2 to be more consistent with theoretical estimates (e.g. Boissoles et al., 2003).

We estimated errors in the ClO VMR retrievals due to uncertainties in the line intensity, γ_{air} and n_{air} of the ClO lines. The typical uncertainties given in Table 1 were used in this error analysis, i.e. 1, 3 and 10 % for the line intensity (Pickett et al., 1998), γ_{air} and n_{air} (Oh and Cohen, 1994, W. G. Read, personal communication, 2011), respectively. As a representative of effects of other molecular transitions, the effect of γ_{air} of the strong O₃ line at 650.732 GHz was evaluated. The wing of this O₃ line contributes largely to baseline of the Band C spectrum. We adopted the γ_{air} of the O₃ line of 3.01 MHz Torr⁻¹ measured by Drouin and Gamache (2008). The error in the ClO VMR due to 3 % uncertainty in the γ_{air} of the O₃ line was estimated. We also estimated the error for the ClO retrieval due to 20 % uncertainty in the dry-air continuum model.

Temperature and pressure for the radiative transfer calculation were taken from the Goddard Earth Observing System Model, Version 5.2 (GEOS-5) (Rienecker et al., 2008) and the Mass Spectrometer and Incoherent Scatter (MSIS) climatology (Hedin, 1991) for the altitude region from the surface to 70 km for the former and that from 70 to 110 km for the latter. Uncertainties in the temperature profile have been conservatively estimated according to the comparison of the temperatures measured from Aura/MLS and GEOS-5 (Schwartz et al., 2008), i.e. 3, 10, 30 and 50 K for the troposphere

Table 1. Spectroscopic parameters of the ClO lines observed by SMILES. The numbers in parentheses represent uncertainties. Intensity is represented by a base-10 logarithm. The quantum numbers are represented by J , Ω , Σ , Λ and F for the total angular momentum, projection of J on the molecular axis (z-axis), projection of the total electron spin momentum on the z-axis, projection of the total orbit momentum on the z-axis and the real total angular momentum including the nuclear spin momentum $I = 3/2$ ($\Omega = \Sigma + \Lambda$, $F = J + I$).

Frequency ^a (GHz)	Intensity ^a (MHz nm ²)	γ^b air (MHz Torr ⁻¹)	n_{air} (-)	Quantum numbers (upper state) ^a					Quantum numbers (lower state) ^a				
				J'	Ω'	Σ'	Λ'	F'	J''	Ω''	Σ''	Λ''	F''
649.44504	-1.9671 (< 1 %)	2.86 (3 %)	0.77 (10 %)	35/2	3/2	1/2	-1	19	33/2	3/2	1/2	+1	18
649.44504	-1.9920 (< 1 %)	2.86 (3 %)	0.77 (10 %)	35/2	3/2	1/2	-1	18	33/2	3/2	1/2	+1	17
649.44504	-2.0170 (< 1 %)	2.86 (3 %)	0.77 (10 %)	35/2	3/2	1/2	-1	17	33/2	3/2	1/2	+1	16
649.44504	-2.0420 (< 1 %)	2.86 (3 %)	0.77 (10 %)	35/2	3/2	1/2	-1	16	33/2	3/2	1/2	+1	15
649.45117	-1.9671 (< 1 %)	2.86 (3 %)	0.77 (10 %)	35/2	3/2	1/2	+1	19	33/2	3/2	1/2	-1	18
649.45117	-1.9920 (< 1 %)	2.86 (3 %)	0.77 (10 %)	35/2	3/2	1/2	+1	18	33/2	3/2	1/2	-1	17
649.45117	-2.0170 (< 1 %)	2.86 (3 %)	0.77 (10 %)	35/2	3/2	1/2	+1	17	33/2	3/2	1/2	-1	16
649.45117	-2.0420 (< 1 %)	2.86 (3 %)	0.77 (10 %)	35/2	3/2	1/2	+1	16	33/2	3/2	1/2	-1	15

^a The JPL catalog version 3 (Pickett et al., 1998). ^b W. G. Read, personal communication, 2011.

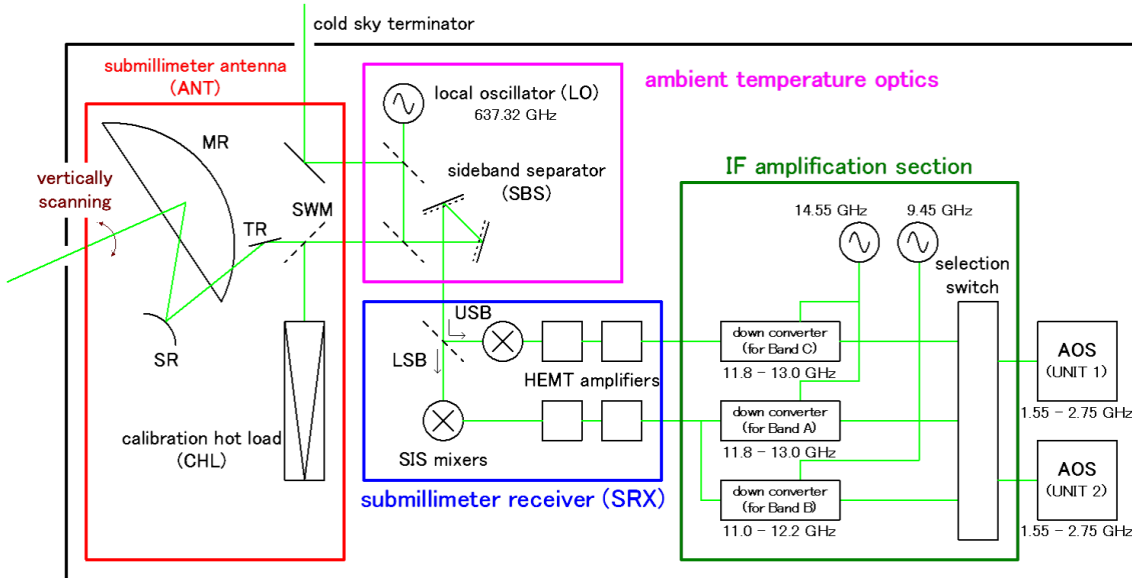


Fig. 2. Schematic of the SMILES payload.

(below 11 km), the stratosphere (11–59 km), the mesosphere (59–96 km) and the thermosphere (above 96 km). The uncertainties in the pressure profile were conservatively set as a constant percentage of 10 % for all altitudes.

2.1.2 Instrument functions

Uncertainty in instrumental parts of forward model

Here, we describe key instrument functions of SMILES such as the antenna beam pattern, the separation ratio of the side-band separator (SBS) and the filter response function of each channel in the spectrometer. Figure 2 shows the signal flow in the SMILES system. Further details on the SMILES

instruments are described by Kikuchi et al. (2010); Masuko et al. (2002) and Ochiai et al. (2012c).

As the optical path of SMILES is well designed to minimize standing waves (the spectral ripple is as small as 0.09 % of input brightness temperature, Ochiai et al., 2012c), their effects were negligible in this error analysis.

The aperture size of the offset Cassegrain antenna (ANT) is 400 mm × 200 mm (Manabe et al., 2012). Its vertical beam size is 0.09°, in terms of the full width at half maximum (FWHM), and the field-of-view is around 3.2–4.0 km at the tangent heights ranging from 10 to 60 km in the condition of the ISS height ranging from 333 to 370 km. Radiance I_v^{ANT} at frequency v received by a boresight solid angle of ANT is given by

$$I_v^{\text{ANT}} = \int_{\Omega_0} I_v(\Omega) R_v^{\text{ANT}}(\Omega) d\Omega, \quad (4)$$

where $I_v(\Omega)$ is the radiance for the direction Ω , R_v^{ANT} is the normalized antenna beam pattern and Ω_0 is the boresight solid angle, defined in the Level-1 processing as the angular range within $\pm 4.2^\circ$ from the boresight direction. The Level-1 brightness temperature does not include the radiance coming from outside Ω_0 , which is estimated and subtracted from the total radiance in the Level-1 processing; more details on related uncertainties are provided below. SMILES periodically scanned atmosphere with a stepping rate of 12 Hz and an angular step of 0.009375° (0.3–0.4 km). The atmospheric limb emissions during six steps in 0.5 s were accumulated to generate a spectrum at one tangent height. The forward model in the L2r v2.1.5 synthesized the spectrum at one tangent height using R_v^{ANT} without adjustments for the antenna movements over six scan steps. The errors in ClO retrieval due to the omission of the adjustments and uncertainty in the beam size were calculated. The beam-size uncertainty used in this error analysis was 2 %, which was conservatively estimated from measurement errors in the pre-launch test of the antenna beam pattern.

Tangent height was geometrically measured from the antenna elevation angle and the ISS attitude. Bias in the measured tangent height was retrieved in the L2r retrieval analysis. Random uncertainty was due to measurement errors of the ISS attitude, and was estimated to be about 0.001° (Ochiai et al., 2012b). It corresponds to 40 m in the tangent height and 0.5 % in the spectrum brightness temperature, which is much smaller than the total random error discussed later. Therefore the error due to the uncertainty in the tangent height was not taken into account in this paper.

Upper sideband (USB) and lower sideband (LSB) were separated using SBS and fed to the SIS mixers for USB and LSB, respectively. The SBS configuration is described by Manabe et al. (2003). The radiance input to the USB mixer ($I_{v_{\text{IF}}}^{\text{UMIX}}$) is expressed using the radiances in the USB ($I_{v_{\text{USB}}}^{\text{ANT}}$) and the LSB ($I_{v_{\text{LSB}}}^{\text{ANT}}$) received by ANT as

$$I_{v_{\text{IF}}}^{\text{UMIX}} = \beta_{v_{\text{IF}}}^{\text{USB}} I_{v_{\text{USB}}}^{\text{ANT}} + (1 - \beta_{v_{\text{IF}}}^{\text{USB}}) I_{v_{\text{LSB}}}^{\text{ANT}}, \quad (5)$$

$$\nu_{\text{IF}} = \nu_{\text{USB}} - \nu_{\text{LO}} = \nu_{\text{LO}} - \nu_{\text{LSB}}, \quad (6)$$

where $\beta_{v_{\text{IF}}}^{\text{USB}}$ is the ratio of the contribution of $I_{v_{\text{USB}}}^{\text{ANT}}$ and ν_{LO} is the frequency of the local oscillator at 637.32 GHz. Ochiai et al. (2008) describe details on $\beta_{v_{\text{IF}}}^{\text{USB}}$. $\beta_{v_{\text{IF}}}^{\text{USB}}$ ranges between 0.98 and 0.99, but it is assumed to be one to reduce a calculation time in the retrieval processing of L2r v2.1.5. We calculated the errors in ClO retrieval due to this assumption and the uncertainty in the $\beta_{v_{\text{IF}}}^{\text{USB}}$ of ± 3 dB.

Two acousto-optical spectrometers (AOSSs), called UNIT 1 and UNIT 2, were used for spectral detection. Response functions of the AOSSs were measured in orbit (Mizobuchi

et al., 2012). UNIT 1 of the AOS was used for ClO observations. The ClO transitions at 649.445 and 649.451 GHz are typically located around AOS channel number 535; the related FWHM of the response function is about 1.06 MHz. The uncertainty in FWHM was conservatively estimated to be 10 %.

Uncertainty in calibration

The Level-1b (L1b) version 007 data were used for processing L2r v2.1.5. Here, we provide a brief overview of the calibration procedure in L1b version 007. After this, we represent radiance I with brightness temperature \mathcal{T} .

The brightness temperature averaged over Ω_0 with a weight of R^{ANT} is denoted as \mathcal{T}_{ANT} . Total brightness temperature \mathcal{T}_{MR} received by ANT at the point of the main reflector (MR) is expressed as

$$\begin{aligned} \mathcal{T}_{\text{MR}} = & \eta_{\text{main}} \mathcal{T}_{\text{ANT}} + \eta_{\text{space}} \mathcal{T}_{\text{B}}(\mathcal{T}_{\text{space}}) \\ & + \eta_{\text{earth}} \mathcal{T}_{\text{B}}(\mathcal{T}_{\text{earth}}) + \eta_{\text{body}} \mathcal{T}_{\text{B}}(\mathcal{T}_{\text{body}}), \end{aligned} \quad (7)$$

where η_{main} is the main beam efficiency in the solid angle region defined by Ω_0 . η_{space} , η_{earth} and η_{body} correspond to fractions of the antenna beam pattern integrated over the solid angles which are directed toward space, the Earth and the SMILES structural body, respectively. $\mathcal{T}_{\text{space}}$, $\mathcal{T}_{\text{earth}}$ and $\mathcal{T}_{\text{body}}$ are the temperatures of space, the Earth and the SMILES structural body, respectively. $\mathcal{T}_{\text{B}}(T)$ represents the brightness temperature of a black body at the temperature T . The main beam efficiency η_{main} is 0.975 in the L1b version 007. We conservatively estimated the uncertainty in η_{main} as 2 %.

The fractional contributions of space, the Earth and the SMILES structural body (η_{space} , η_{earth} and η_{body} , respectively) were geometrically calculated as

$$\begin{aligned} \eta_{\text{space}} &= 0.084(1 - \eta_{\text{main}}), \\ \eta_{\text{earth}} &= 0.060(1 - \eta_{\text{main}}), \\ \eta_{\text{body}} &= 0.856(1 - \eta_{\text{main}}), \end{aligned} \quad (8)$$

for the Earth's limb observations, and

$$\begin{aligned} \eta_{\text{space}} &= 0.140(1 - \eta_{\text{main}}), \\ \eta_{\text{earth}} &= 0.004(1 - \eta_{\text{main}}), \\ \eta_{\text{body}} &= 0.856(1 - \eta_{\text{main}}), \end{aligned} \quad (9)$$

for the cold-reference measurements (cosmic microwave background). We assumed in the L1b version 007 processing that $\mathcal{T}_{\text{B}}(\mathcal{T}_{\text{space}})$ was substantially 0 K, $\mathcal{T}_{\text{earth}}$ was 255 K, and $\mathcal{T}_{\text{body}}$ was the measured physical temperature of the antenna structure. $\mathcal{T}_{\text{earth}}$ had the largest variations for $\mathcal{T}_{\text{space}}$, $\mathcal{T}_{\text{earth}}$ and $\mathcal{T}_{\text{body}}$. We investigated errors due to uncertainties in the $\mathcal{T}_{\text{earth}}$ of 20 K (typical variations in the Earth's actual atmosphere).

Joule mirror losses were taken into account in this error analysis. Brightness temperatures due to losses of the main reflector (MR), the sub-reflector (SR) and the tertiary reflector (TR) were not calibrated, although a reference brightness

temperature from the calibration hot load (CHL) was measured every 53 s by inserting the switching mirror (SWM) in the beam at switching point between the TR and the fourth reflector. Brightness temperature $T_{\text{TR}}^{\text{atm}}$ of the beam at the switching point for the atmospheric measurements is expressed as

$$T_{\text{TR}}^{\text{atm}} = \mu_{\text{MR}} \mu_{\text{SR}} \mu_{\text{TR}} T_{\text{MR}} + (1 - \mu_{\text{MR}} \mu_{\text{SR}} \mu_{\text{TR}}) T_{\text{B}}(T_{\text{mirror}}), \quad (10)$$

where μ_{MR} , μ_{SR} and μ_{TR} are the transmission coefficients of MR, SR and TR, respectively, and T_{mirror} is the temperature of the reflectors. These three reflectors were assumed to be at the same temperature T_{mirror} , because the mirrors were made from highly thermally conducting material (aluminum alloy) (Manabe et al., 2012). Scattering and spillover losses at these reflectors were counted in the efficiency η_{body} and not in μ_{MR} , μ_{SR} or μ_{TM} . Brightness temperature $T_{\text{TR}}^{\text{hot}}$ of the beam for the hot-reference brightness temperature at TR is

$$T_{\text{TR}}^{\text{hot}} = \mu_{\text{SWM}} \{ \mu_{\text{CHL}} T_{\text{B}}(T_{\text{CHL}}) + (1 - \mu_{\text{CHL}}) T_{\text{RX}} \} + (1 - \mu_{\text{SWM}}) T_{\text{B}}(T_{\text{mirror}}), \quad (11)$$

where μ_{SWM} is the transmission coefficient of SWM, μ_{CHL} is one minus the reflection coefficient of CHL, T_{CHL} is the temperature of CHL and T_{RX} is brightness temperature of incident to CHL. The coefficients μ_{MR} , μ_{SR} , μ_{TR} and μ_{SWM} are 0.9955, 0.9958, 0.9956 and 0.9959, respectively. These values were estimated from laboratory reflection measurements of materials that have identical surfaces as reflectors. Uncertainties in these coefficients were estimated to be 0.1 %. A power reflection coefficient of CHL was negligibly small (less than -60 dB), and μ_{CHL} was assumed to be one.

The receiver output, i.e. the quantized output from AOS, deviates from a linear relation to the input brightness temperature because of gain nonlinearity of the receiver and the spectrometer components. Output V_{ν} from AOS at the channel corresponding to the frequency ν is given by

$$V_{\nu} = G_{\nu} (1 - \alpha \bar{V} - \alpha' V_{\nu}) p_{\nu} + V_0, \quad (12)$$

where G_{ν} is the total system gain, \bar{V} is the average of V_{ν} over all spectrometer channels, V_0 is the offset of the AOS output, and p_{ν} is the total input power to the receiver. \bar{V} was assumed to be 12 000 and 22 500 for the cold and hot references, respectively, in this error analysis. The input power p_{ν} is proportional to a sum of T_{ANT} and system noise temperature T_{sys} ; T_{sys} includes system noise, the brightness coming from direction Ω_0 and the emissions from the lossy reflectors. Coefficients α and α' represent receiver gain nonlinearity (Ochiai et al., 2012a). α was 1.884×10^{-6} and was measured in the pre-launch test. We call α a “gain-compression parameter”. We conservatively estimated uncertainty in α as 20 % including errors from the signals outside the spectrometer passbands. The term $\alpha' V_{\nu}$ did not have large effects on the ClO retrieval compared with the term $\alpha \bar{V}$ and was ignored in this error analysis.

The Level-1 processing produces brightness temperature spectrum y_{obs} , which is the estimation of T_{ANT} using V_{ν} for the atmospheric limb observations, the cold (space) and hot (CHL) references. These cold and hot references were measured every 53 s (Ochiai et al., 2008).

2.2 Inversion analysis

We employed the optimal estimation method (Rodgers, 2000) for the L2r retrieval analysis of version 2.1.5 (Baron et al., 2011). The method leads to the maximum a posteriori solution, which minimizes the value of χ^2 :

$$\chi^2 = [y_{\text{obs}} - \mathcal{F}(\mathbf{x}, \mathbf{b})]^T \mathbf{S}_y^{-1} [y_{\text{obs}} - \mathcal{F}(\mathbf{x}, \mathbf{b})] + (\mathbf{x} - \mathbf{x}_a)^T \mathbf{S}_a^{-1} (\mathbf{x} - \mathbf{x}_a), \quad (13)$$

where \mathcal{F} is the forward model, \mathbf{x} is the vector of the atmospheric true state, and \mathbf{b} is the vector of the parameters used in \mathcal{F} . \mathbf{S}_y is the covariance matrix for spectrum noise ϵ_y , \mathbf{x}_a is the a priori state of \mathbf{x} and \mathbf{S}_a is the covariance matrix for the natural variability of \mathbf{x} . We use \mathbf{S}_y and \mathbf{S}_a as tuning parameters to obtain a stable retrieval.

$$\mathbf{S}_y[i, j] = \epsilon_y^2 \delta_{i,j}, \quad \epsilon_y = 0.5 \text{ K}, \quad (14)$$

where $\delta_{i,j}$ is the Kronecker delta.

$$\mathbf{S}_a[i, j] = \epsilon_a[i] \epsilon_a[j] \exp \left[-\frac{|z[i] - z[j]|}{z_c} \right], \quad (15)$$

$$\epsilon_a[i] = \epsilon_1 \mathbf{x}_a[i] + \epsilon_2, \quad (\epsilon_1, \epsilon_2) = (0.5, 2.0 \times 10^{-10}) \quad (16)$$

where z_c is the correlation length that constrains the vertical continuity in the retrieved profile, and is set to be 6 km.

A vertical VMR profile of ClO was retrieved using each scan of the Band C spectrum with a reduced frequency window of 649.4 ± 0.2 GHz. The ClO a priori profile was the same as that for Odin/SMR, which was based on the UARS/MLS climatology. The weighting functions (see Eq. 22) were calculated at altitudes from 16 to 43 km with 3-km intervals, from 43 to 55 km with 4-km intervals and from 55 to 95 km with 5-km intervals. We used the measurement spectra whose tangent heights range from 15 to 90 km. The accompanying retrieval parameters were a second-order polynomial baseline, an offset of the AOS frequency and a line-of-sight elevation angle for each scan. Although the offset of the line-of-sight elevation angle was also retrieved using the O₃ line in Bands A and B (Baron et al., 2011), the offset used for the ClO retrieval was independently retrieved using the ClO lines and the baseline spectra in Band C. The pointing information came from the pressure broadening of the line in combination with the assumed a priori knowledge in the background atmosphere. The temperature and pressure profiles were not retrieved in the Band C retrieval. The VMR of H₂O was also set as a variable with an intention of improving the fit of the baseline.

2.3 Method of error calculation

Total error $\mathbf{E}_{\text{total}}$ is given by

$$\mathbf{E}_{\text{total}}[i] = \sqrt{\mathbf{E}_{\text{noise}}^2[i] + \mathbf{E}_{\text{smooth}}^2[i] + \mathbf{E}_{\text{param}}^2[i] + \mathbf{E}_{\text{calib}}^2[i]}, \quad (17)$$

where $\mathbf{E}_{\text{noise}}$ is the error due to spectrum noise, $\mathbf{E}_{\text{smooth}}$ is the smoothing error, $\mathbf{E}_{\text{param}}$ is the error due to uncertainties in the model parameters and $\mathbf{E}_{\text{calib}}$ is the error due to inaccuracies in the spectrum calibration. We conservatively estimated the uncertainties for each error source described in Sects. 2.1 and 2.2. We took the root-sum-square values for the estimation of the total systematic error, since we considered as many (16) error sources as possible and most of the error sources were conservatively estimated.

We assumed that the true state was identical to the a priori state \mathbf{x}_a , and synthesized reference spectrum \mathbf{y}_{ref} using \mathbf{x}_a . Inversion calculation was performed using \mathbf{y}_{ref} . We used retrieved state \mathbf{x}_{ref} (not \mathbf{x}_a) as a reference profile for this error analysis as this removed the characteristics included in the retrieval algorithm itself.

$$\mathbf{x}_{\text{ref}} = \mathcal{I}(\mathbf{y}_{\text{ref}}, \mathbf{b}_0), \quad (18)$$

where \mathcal{I} is the inversion function and \mathbf{b}_0 is the vector of model parameters. The reference profile is shown in Fig. 3 with the difference in \mathbf{x}_a and \mathbf{x}_{ref} . This figure also shows measurement response \mathbf{m} and averaging kernel \mathbf{A} . Details on \mathbf{m} are explained by Baron et al. (2002), and we simplified them as

$$\mathbf{m}[i] = \sum_j |\mathbf{A}[i, j]|, \quad (19)$$

$$\mathbf{A} = \frac{\partial \hat{\mathbf{x}}}{\partial \mathbf{x}} = \mathbf{D}\mathbf{K}, \quad (20)$$

$$\mathbf{D} = \frac{\partial \hat{\mathbf{x}}}{\partial \mathbf{y}} = (\mathbf{K}^T \mathbf{S}_y^{-1} \mathbf{K} + \mathbf{S}_a^{-1})^{-1} \mathbf{K}^T \mathbf{S}_y^{-1}, \quad (21)$$

$$\mathbf{K} = \frac{\partial \mathbf{y}}{\partial \mathbf{x}}, \quad (22)$$

where $\hat{\mathbf{x}}$ was a solution of the retrieval. Weighting function \mathbf{K} was analytically calculated. \mathbf{m} , \mathbf{A} and contribution function \mathbf{D} were consecutively given using \mathbf{K} (Urban et al., 2004). Typical vertical resolutions of L2r version 2.1.5 were about 3–5 and 5–8 km for altitude regions of 30–50 and 50–70 km, respectively.

2.3.1 Retrieval error

Retrieval error consists of the error due to spectrum statistical noise $\mathbf{E}_{\text{noise}}$ and the smoothing error $\mathbf{E}_{\text{smooth}}$.

$$\begin{aligned} \mathbf{S}_{\text{noise}} &= \mathbf{D}\mathbf{S}_y\mathbf{D}^T, \\ \mathbf{E}_{\text{noise}}[i] &= \sqrt{\mathbf{S}_{\text{noise}}[i, i]}, \end{aligned} \quad (23)$$

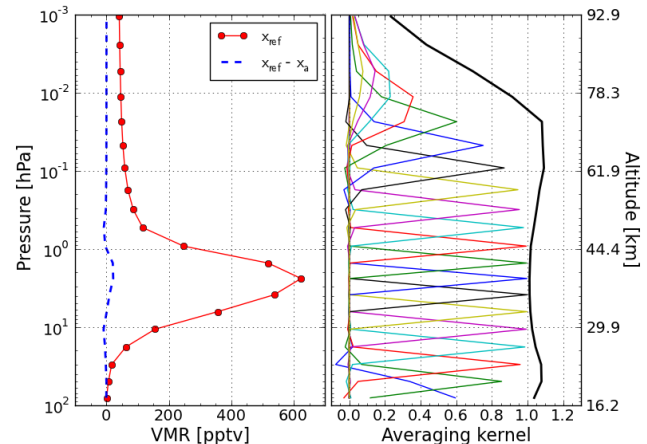


Fig. 3. Reference profile \mathbf{x}_{ref} of ClO VMR used in the error analysis. The left figure shows \mathbf{x}_{ref} and the difference in \mathbf{x}_a and \mathbf{x}_{ref} . The right figure shows the measurement response (black solid line) and the averaging kernels.

where $\mathbf{S}_{\text{noise}}$ is the error covariance matrix for measurement noise.

$$\begin{aligned} \mathbf{S}_{\text{smooth}} &= (\mathbf{A} - \mathbf{U})\mathbf{S}_a(\mathbf{A} - \mathbf{U})^T, \\ \mathbf{E}_{\text{smooth}}[i] &= \sqrt{\mathbf{S}_{\text{smooth}}[i, i]}, \end{aligned} \quad (24)$$

where $\mathbf{S}_{\text{smooth}}$ is the error covariance matrix for errors derived from \mathbf{S}_a and \mathbf{U} is the unit matrix. Note that $\mathbf{E}_{\text{smooth}}$ has both aspects for being included in random error ($\mathbf{E}_{\text{random}}$) and systematic error ($\mathbf{E}_{\text{systematic}}$). The random aspect in $\mathbf{E}_{\text{smooth}}$ results from applying a finite vertical retrieval grid to true state \mathbf{x} . The systematic aspect arises by making $\hat{\mathbf{x}}$ to be identical to \mathbf{x}_a where the measurement response \mathbf{m} is low. We focused on the data of L2r version 2.1.5 that satisfy $\mathbf{m} > 0.8$ in this paper, where $\mathbf{E}_{\text{smooth}}$ was more random than systematic. We categorized $\mathbf{E}_{\text{smooth}}$ as $\mathbf{E}_{\text{random}}$ in the following study.

2.3.2 Uncertainty in model parameters

Errors due to the uncertainties in the spectroscopic parameters, the instrument functions and the atmospheric profiles of temperature and pressure are categorized into $\mathbf{E}_{\text{param}}$. $\mathbf{E}_{\text{param}}$ is calculated as

$$\mathbf{E}_{\text{param}} = \mathcal{I}(\mathbf{y}_{\text{ref}}, \mathbf{b}_0 + \Delta\mathbf{b}) - \mathcal{I}(\mathbf{y}_{\text{ref}}, \mathbf{b}_0), \quad (25)$$

where \mathbf{y}_{ref} is the reference spectrum and \mathbf{b}_0 is a vector of model parameters.

We took into account vertical correlations for the error calculations of the uncertainties in the atmospheric temperature and pressure profiles. We calculated the ClO errors due to the temperature and pressure profiles employing singular value decomposition as follows. The model parameter \mathbf{b}_0 has correlated uncertainty $\Delta\mathbf{b}$. \mathbf{b}_0 is represented with respect to the

Table 2. Summary of the error sources for a single-scan observation.

Systematic (S) or Random (R)	Error source	Uncertainty in error source	Error at 2.5 hPa (pptv)	Calculation method
R	Spectrum noise	ϵ_y^1	14	Eq. (23)
R	Smoothing error	ϵ_a^2	2.9	Eq. (24)
R	Temperature profile	footnote ³	9.2	Eq. (25)
R	Pressure profile	10 %	20	Eq. (25)
S	Line intensity ⁴	1 %	6.3	Eq. (25)
S	γ_{air} (Air-broadening coefficient) ⁴	3 %	17	Eq. (25)
S	n_{air} (Temperature dependence of γ_{air}) ⁴	10 %	15	Eq. (25)
S	γ_{air} of the O ₃ line at 650.732 GHz	3 %	0.022	Eq. (25)
S	Dry-air continuum	20 %	3.5	Eq. (25)
S	Antenna beam pattern	footnote ⁵	3.8	Eq. (25)
S	SBS characteristics	footnote ⁶	0.13	Eq. (25)
S	AOS response function	10 % in FWHM	0.24	Eq. (25)
S	Gain-compression parameter α	20 %	6.2	Eq. (31)
S	Main beam efficiency η_{main}	2 %	1.9	Eq. (31)
S	Joule loss of mirrors μ	0.1 %	0.042	Eq. (31)
S	Temperature of the Earth T_{earth}	20 K	0.010	Eq. (31)

¹ Given by Eq. (14). ² Given by Eq. (16). ³ 3 K in the troposphere, 10 K in the stratosphere, 30 K in the mesosphere and 50 K in the thermosphere. ⁴ Of the ClO lines at 649.445 and 649.451 GHz. ⁵ 2 % uncertainty in FWHM of R^{ANT} and no adjustment of six steps in one tangent height. ⁶ Assuming $\beta^{\text{USB}} = 1$ and $\pm 3 \text{ dB}$ in β^{USB} .

eigenfunctions of covariance matrix \mathbf{S}_b to obtain a representation of \mathbf{b}_0 with uncorrelated components, called $\bar{\mathbf{b}}_0$, using orthogonal matrix \mathbf{B} ($\mathbf{B}\mathbf{B}^T = \mathbf{U}$).

$$\mathbf{b}_0 = \mathbf{B}\bar{\mathbf{b}}_0, \quad \bar{\mathbf{b}}_0 = \mathbf{B}^T \mathbf{b}_0. \quad (26)$$

A covariance matrix of $\bar{\mathbf{b}}_0$ ($\mathbf{S}_{\bar{b}}$) is a diagonal matrix and composed of the eigenvalues of \mathbf{S}_b . $\mathbf{S}_{\bar{b}}$ is expressed using \mathbf{S}_b and \mathbf{B} as

$$\mathbf{S}_{\bar{b}} = \mathbf{B}^T \mathbf{S}_b \mathbf{B}. \quad (27)$$

The covariance matrix of the temperature uncertainties is expressed as

$$\mathbf{S}_b[i, j] = \epsilon_T[i] \epsilon_T[j] \exp \left\{ -\frac{(z[i] - z[j])^2}{2z_c'^2} \right\}, \quad (28)$$

where $\epsilon_T[i]$ is the temperature uncertainty at i -th altitude $z[i]$. z_c' is the correlation length and is set to be 6 km (the same as z_c in Eq. 15). $\mathbf{S}_{\bar{b}}$ and \mathbf{B} are computed from \mathbf{S}_b using numerical linear algebra packages. The ClO VMR error $\epsilon_{\text{param}}^i$ due to the uncertainty at the i -th altitude level is given by

$$\epsilon_{\text{param}}^i = \mathcal{I} \left(\mathbf{y}_{\text{ref}}, \mathbf{b}_0 + \sqrt{\mathbf{S}_{\bar{b}}[i, i]} \mathbf{B}^i \right) - \mathcal{I}(\mathbf{y}_{\text{ref}}, \mathbf{b}_0), \quad (29)$$

where \mathbf{B}^i is the i -th row vector of \mathbf{B} . All $\epsilon_{\text{param}}^i$ values are added by taking the root-sum-square.

$$\epsilon_{\text{param}}[i] = \sqrt{\sum_j \epsilon_{\text{param}}^j[i]^2}. \quad (30)$$

2.3.3 Calibration inaccuracy

Errors due to the inaccuracies in the spectrum calibration $\mathbf{E}_{\text{calib}}$ are calculated as

$$\mathbf{E}_{\text{calib}} = \mathbf{D} \Delta \mathbf{y}, \quad (31)$$

where $\Delta \mathbf{y}$ is the difference between the values using the calibration parameter from L1b processing and that with the added uncertainty.

3 Results of error analysis

Error analysis was carried out for all possible error sources listed in Table 2. We separately discuss the results obtained from the error analysis for the random error $\mathbf{E}_{\text{random}}$ and the systematic error $\mathbf{E}_{\text{systematic}}$. $\mathbf{E}_{\text{random}}$ can be decreased by averaging several profiles; on the other hand, $\mathbf{E}_{\text{systematic}}$ remains constant. $\mathbf{E}_{\text{random}}$ consists of $\mathbf{E}_{\text{noise}}$, $\mathbf{E}_{\text{smooth}}$ and $\mathbf{E}_{\text{param}}$ due to the uncertainties in the temperature and pressure profiles. $\mathbf{E}_{\text{systematic}}$ consists of $\mathbf{E}_{\text{param}}$ due to the uncertainties in the spectroscopic parameters, the instrument functions and $\mathbf{E}_{\text{calib}}$. Total error for averaging N profiles is given by

$$\mathbf{E}_{\text{total}}(N)[i] = \sqrt{\mathbf{E}_{\text{systematic}}^2[i] + \frac{\mathbf{E}_{\text{random}}^2(1)[i]}{N}}, \quad (32)$$

where $\mathbf{E}_{\text{random}}(1)$ is the random error for a single-scan observation.

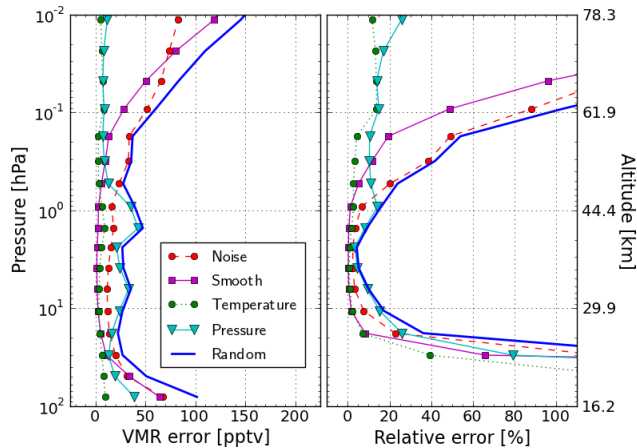


Fig. 4. Summary of the random errors for a single-scan observation. Red: E_{noise} . Purple: E_{smooth} . Green: error from temperature profile; the uncertainties are 3, 10, 30 and 50 K for the troposphere (below 11 km), the stratosphere (11–59 km), the mesosphere (59–96 km) and the thermosphere (above 96 km). Cyan: error from pressure profile (10 %). Blue: total random error.

3.1 Random error

Figure 4 shows the error budgets for E_{random} , i.e. E_{noise} , E_{smooth} and E_{param} for the temperature and pressure profiles. This paper presents both absolute VMR errors (left) and relative errors (right) for all results in the error calculations. Relative errors were calculated as absolute VMR errors divided by x_{ref} . E_{noise} and E_{smooth} were less than 20 % at pressures between 0.6 and 20 hPa where the CIO VMR was enhanced. The errors in the CIO retrieval due to the uncertainties in the atmospheric temperature and pressure profiles were calculated employing singular value decomposition (Eq. 30). The errors due to the temperature profile were within 5 % at pressures between 0.2 and 20 hPa and increased at pressures larger than 10 hPa, even though there were smaller uncertainties at these lower altitudes. The errors due to the pressure profile were increased to more than 50 % at pressures larger than 2 hPa and were almost constant at 10–20 % at pressures smaller than 2 hPa. The temperature and pressure profiles are related to several other parameters such as γ_{air} and n_{air} , which increases the contribution of the uncertainties in the temperature and pressure profiles to the CIO retrieval.

The total random error was given by the root-sum-square of the retrieval errors and the errors due to the temperature and pressure profiles. At pressures smaller than 0.1 hPa, the retrieval errors were dominant and E_{random} was increased from 50 to 200 pptv ($> 100 \%$). E_{random} was about 30–50 pptv at pressures larger than 0.1 hPa. The pressure profile made the largest contribution to the random error in the stratosphere.

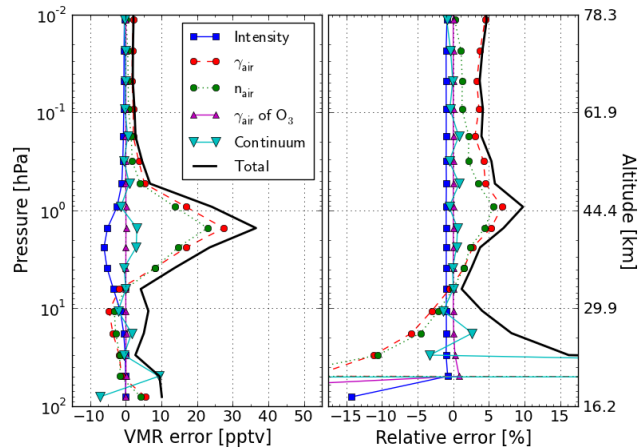


Fig. 5. Same as Fig. 4 except for the errors from the spectroscopic parameters. Blue: +1 % uncertainty in line intensity, red: +3 % uncertainty in γ_{air} , and green: +10 % uncertainty in n_{air} of the CIO transitions at 649.445 and 649.451 GHz. Purple: +3 % uncertainty in γ_{air} for the O_3 transition at 650.732 GHz. Cyan: +20 % uncertainty in the dry-air continuum. Black: total error for the five components.

3.2 Systematic error

3.2.1 Error due to uncertainty in spectroscopic parameters

Figure 5 shows the error budgets for the spectroscopic parameters. The bold black line represents the total error calculated as the root-sum-square values for the spectroscopic parameters we investigated. The total error is around 4 % at the pressures smaller than 0.05 hPa. The largest contribution comes from the uncertainty in γ_{air} for those from the spectroscopic parameters. The error due to the 3 % uncertainty in γ_{air} is about 5 % for all pressures, and the maximum is 27 pptv (8 %) at around 1 hPa. We can see that the sign of VMR difference reverses at around 7 hPa. When γ_{air} is larger, intensity around the center of the line of the synthesized spectrum is lower while the intensities in the wings are higher. The CIO VMR at larger pressures is retrieved from the wings of the CIO lines, whereas that at smaller pressures is derived from the center of the line. Rate of contributions from the center of the line versus those from the wings increases with altitude. Therefore, a smaller VMR is retrieved at larger pressures and larger VMR is retrieved at smaller pressures, by using a larger value of γ_{air} .

The error from n_{air} follows that from γ_{air} . The vertical trends in the errors from γ_{air} and n_{air} are similar. According to the definition of Eq. (3), increasing n_{air} increases γ_{air} in the atmosphere whose temperature is lower than 296 K. Such temperature conditions are satisfied at most altitudes observed by SMILES. The uncertainty in the line intensity almost straightforwardly propagates to the error in the CIO VMR at pressures smaller than 50 hPa, but with an opposite

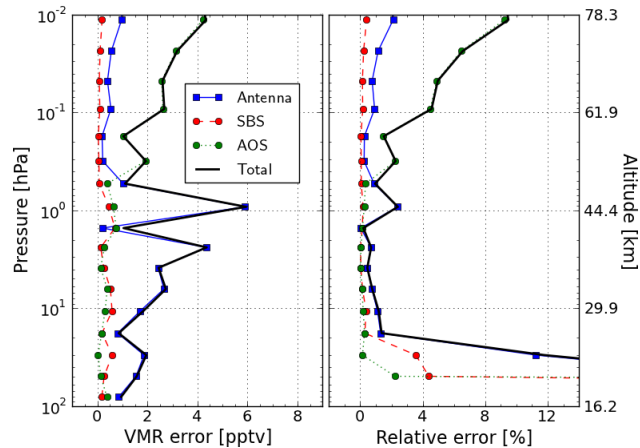


Fig. 6. Same as Fig. 4 except for errors from the instrument functions in the forward model. Blue: error from the antenna beam pattern. Red: error from the SBS. Green: 10 % uncertainty in the width of the AOS response function. Black: total error of three components.

sign; i.e., +1 % uncertainty in the line intensity results in about –1 % relative error. The error from the dry-air continuum model increased to more than 10 % at the pressures larger than 10 hPa. The continuum model affects the baseline correction in the retrieval particularly at larger pressures. The spectral line shape of ClO broadens as pressure increases, which makes it more difficult to distinguish the ClO signals and the baseline. The error due to the uncertainty in γ_{air} of the ozone line at 650.732 GHz is negligibly small.

3.2.2 Error due to uncertainty in instrument functions

Uncertainty in instrument-related parts of forward model

Figure 6 shows the error budgets for the instrument functions in the forward model, i.e. the antenna beam patterns and the characteristics of SBS and the AOS response functions. The bold black line represents the total error calculated as the root-sum-square value of the errors from the three instrument functions. The total error is less than 4 % at the pressures between 0.1 and 10 hPa. A dominant factor is the AOS response function at the pressures smaller than 0.3 hPa. The ClO retrieval at smaller pressures is more sensitive to the AOS response function since the spectral line width becomes comparable to or smaller than the width of the AOS response function.

The error from the ANT is the largest of the instrument functions between 0.6 and 10 hPa. We individually calculated the errors due to the 2 % uncertainty in the beam size and the lack of the adjustment of the antenna movements during the data integration time for the measurement spectrum at one tangent height. The error from the ANT plotted in Fig. 6 is the root-sum-square value of these two errors. It seems that

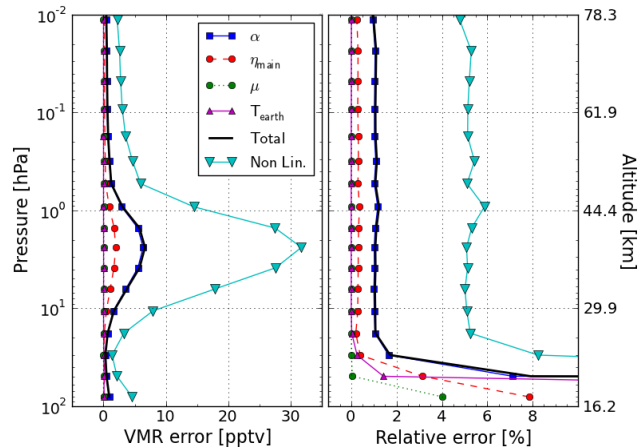


Fig. 7. Same as Fig. 4 except for the uncertainty in the calibration parameters. Blue: 20 % uncertainty in the gain-compression parameter α . Red: 2 % uncertainty in the main beam efficiency η_{main} . Green: total error due to 0.1 % uncertainties in the Joule losses μ for mirrors (MR, SR, TR and SWM). Purple: 20 K uncertainty in the temperature of the Earth T_{earth} . Black: total error due to the inaccuracies of the spectrum calibration. Cyan: error due to nonlinearity being neglected between brightness temperature \mathcal{T} and AOS output V .

the error from the ANT oscillates between 3 and 1 hPa, although the amplitude is small (about 6 pptv). The error from the SBS is the root-sum-square value of the errors due to the ± 3 dB uncertainty in β^{USB} and assuming $\beta^{\text{USB}} = 1$ in the L2r retrieval processing. The error from the SBS has the smallest contribution of the three instruments.

Uncertainty in spectrum calibration

Figure 7 shows the error budgets due to the uncertainties in the calibration parameters, i.e. the gain-compression parameter α , the main beam efficiency η_{main} , the Joule losses of the mirrors μ and the temperature of the Earth T_{earth} . The total error is given by the root-sum-square of the errors due to the uncertainties in these calibration parameters, and it is about 1 % between 0.01 and 20 hPa. The error from α is the largest and is followed by that from η_{main} . The error from μ is given by the root-sum-square of the individually calculated errors in the 0.1 % uncertainties in the Joule losses of MR, SR, TR and SWM. The errors from μ and T_{earth} are negligible.

We calculated the effect by taking into account nonlinearity between the AOS output V and the brightness temperature \mathcal{T} , which is indicated by the cyan line in Fig. 7 labeled “Non Lin.”. Note that it is not included in the total error of the ClO retrieval in this error analysis. It makes a contribution as large as approximately 5 % relative error, which is about five times that of the total error from the uncertainties in the calibration parameters. This clearly indicates that it is essential to carefully consider the nonlinearity between V and \mathcal{T} in the spectrum calibration.

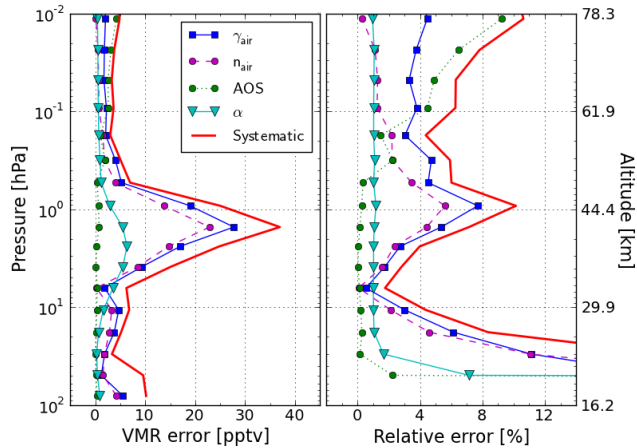


Fig. 8. Same as Fig. 4 except for the systematic error. The total systematic error and the errors from the main error sources are shown. Blue: 3 % uncertainty in γ_{air} . Purple: 10 % uncertainty in n_{air} . Green: 10 % uncertainty in the width of the AOS response function. Cyan: 20 % uncertainty in α . Red: total systematic error.

3.2.3 Summary of systematic error

Figure 8 shows $E_{\text{systematic}}$ and its main components such as the errors due to the uncertainties in the γ_{air} and n_{air} of the CIO transition, the width of the AOS response function and α . $E_{\text{systematic}}$ is smaller than 10 pptv at all pressures except for around 1 hPa, where the CIO VMR is increased. The uncertainties in γ_{air} and n_{air} are dominant in the region of pressure larger than 0.1 hPa. The error from the AOS response function is the largest followed by that from γ_{air} at the pressures less than 0.1 hPa. The gain-compression parameter (α) has the largest of among the calibration parameters, but the error from α is smaller than the other errors in Fig. 8.

There is a peak at about 2 hPa (40 km) in the VMR error. This may be because of the assumed CIO VMR profile, i.e. the a priori profile x_a , which has VMR maximum at 40 km. The errors due to the uncertainties in γ_{air} and n_{air} , which are the large error sources in $E_{\text{systematic}}$, depend on the retrieved VMR value. The value of x_a decreases rapidly at the pressures less than 2 hPa (40 km), and the peak of the relative error is located at about 1 hPa (45 km).

Overall, the error due to γ_{air} makes the largest contribution to $E_{\text{systematic}}$. The uncertainties in laboratory measurements of γ_{air} are difficult to be reduced because of experimental systematic errors such as errors in measurements of pressure, difficulties of maintaining stable temperature conditions during measurements (Sato et al., 2010), and contaminations with undesirable species (Oh and Cohen, 1994), for example. Moreover, no theoretical prediction of γ_{air} has yet been completely established. We concluded that the uncertainty in γ_{air} was one of the largest error sources in the CIO retrieval.

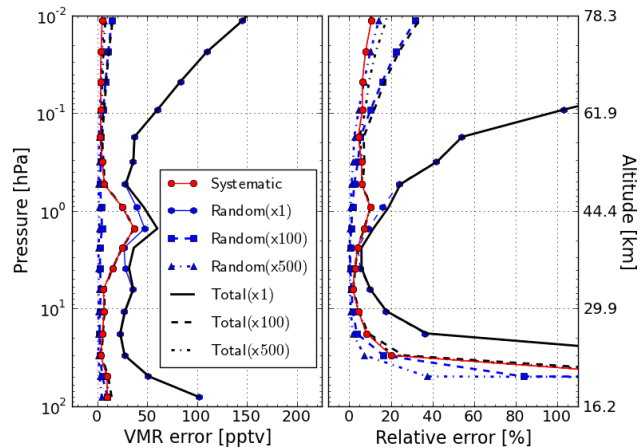


Fig. 9. Same as Fig. 4 except for the total error. Total error in the CIO retrieval for averaging of N profiles ($N = 1, 100$ and 500). Red: systematic error. Blue: random error when averaging N profiles. Black: total error when averaging N profiles.

3.3 Total error

Figure 9 shows E_{random} , $E_{\text{systematic}}$ and E_{total} for a single-scan observation and averaging of N ($= 100, 500$) profiles. E_{random} is larger than $E_{\text{systematic}}$ for a single-scan observation, and is dominant in E_{total} at all pressures. Averaging 100 profiles, $E_{\text{random}}(100)$ is less than 10 pptv (10 %) at pressures larger than 0.2 hPa. $E_{\text{systematic}}$ is dominant in $E_{\text{total}}(100)$ in this pressure region. $E_{\text{random}}(100)$ is still as large as 10–20 pptv in the pressure region smaller than 0.2 hPa. When 500 profiles are averaged, $E_{\text{random}}(500)$ is less than 10 pptv (20 %) at all pressures.

We compared the errors in the CIO VMR of the SMILES L2r (v2.1.5) estimated in this work, those in UARS/MLS (v5) by Livesey et al. (2003), Aura/MLS (v3-3) by Livesey et al. (2011), and Odin/SMR (Chalmers v2.1) by Urban et al. (2006). The systematic errors, the random errors ($1-\sigma$) for a single-scan observation and the vertical resolutions at 0.5, 2 and 10 hPa are summarized in Table 3. The systematic errors of SMILES, UARS/MLS and Aura/MLS are of the same order 10–50 pptv. The random errors of SMILES are about a tenth of those with the other instruments because of the low-noise spectra observed using the SIS mixers. The vertical resolutions of SMILES are comparable to those of Aura/MLS and Odin/SMR.

4 CIO diurnal variations

4.1 Evaluation of SMILES CIO diurnal variations

Figure 10 shows the diurnal variations in SMILES zonal mean CIO for mid-latitude (40° N– 50° N) and equatorial (5° S– 5° N) regions at the pressures of 10 hPa (30 km), 4.6 hPa (35 km), 2.1 hPa (41 km), 1 hPa (47 km), 0.46 hPa

Table 3. Summary of the errors ($1-\sigma$) for a single-scan observation of ClO products observed by SMILES, UARS/MLS, Aura/MLS and Odin/SMR. Systematic error (SE), random error (RE) and vertical resolution (VR) for these instruments are listed.

Pressure (Altitude)	SMILES L2r (v2.1.5) ¹			UARS/MLS (v5) ²			Aura/MLS (v3-3) ³			Odin/SMR (Chalmers v2.1) ⁴		
	SE (pptv)	RE (pptv)	VR (km)	SE (pptv)	RE (pptv)	VR (km)	SE (pptv)	RE (pptv)	VR (km)	SE (pptv)	RE (pptv)	VR (km)
0.5 hPa (50 km)	10	30	5.5	—	—	—	—	—	—	≤ 100	≤ 150	2.5–3
2 hPa (40 km)	30	40	4	60	400	6	25	100	3.5–4.5	≤ 100	≤ 150	2.5–3
10 hPa (30 km)	10	30	4	30	400	4	20	100	3.5–4.5	≤ 100	≤ 150	2.5–3

¹ This work. ² See Table 9 in Livesey et al. (2003). ³ See Table 3.5.1 in Livesey et al. (2011). ⁴ See Table 1 in Urban et al. (2006).

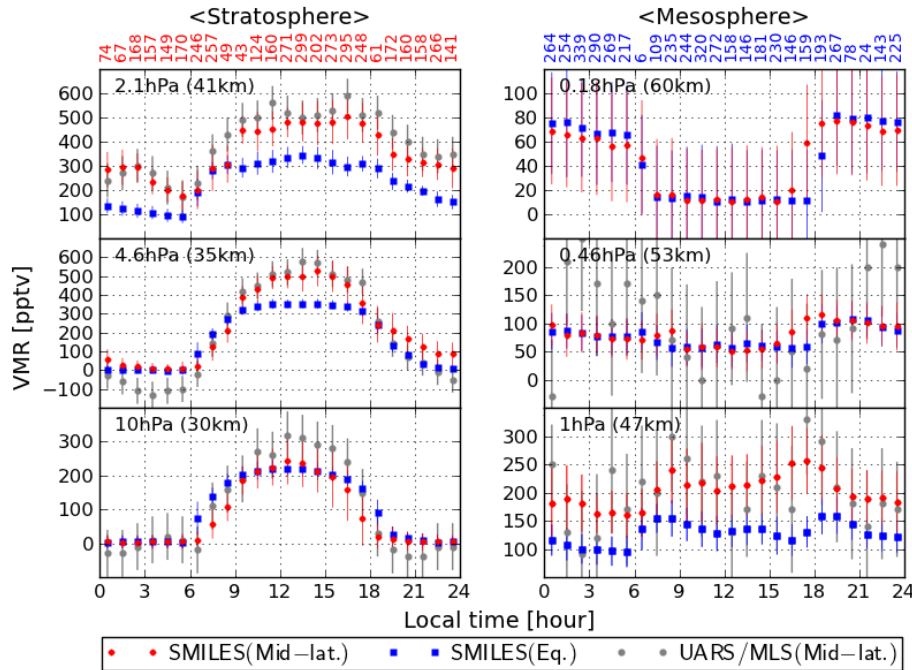


Fig. 10. ClO diurnal variations observed by SMILES and UARS/MLS at pressures of 0.18, 0.46, 1, 2.1, 4.6 and 10 hPa for zonal mean. Red: SMILES at 40° N– 50° N. Blue: SMILES at 5° S– 5° N. Gray: UARS/MLS at 40° N– 50° N. The data are averaged within a local time bin of 1-h intervals. The vertical error bars represent $1-\sigma$ standard deviations. The numbers of profiles averaged at each local time for the SMILES observations at 40° N– 50° N and 5° S– 5° N are indicated at the top of the left and right panels, respectively. The vertical grids for SMILES were adjusted to the UARS/MLS grids with linear interpolation. The SMILES data are taken for the observation period from January to February 2010, while UARS/MLS data are taken by averaging February data for the seven years from 1991 to 1997. The UARS/MLS data are taken from Fig. 1 in Ricaud et al. (2000). Arbitrary offsets are respectively added to the UARS/MLS data of 100, 200, 400, 200 and 100 pptv at 0.46, 1, 2.1, 4.6 and 10 hPa, since the UARS/MLS data have a negative bias.

(53 km) and 0.18 hPa (60 km). Two months of data from the SMILES observations were averaged from January–February in 2010. Criteria for data selection were measurement response > 0.8 (Eq. 19) and $\chi^2 < 1$ (Eq. 13). The numbers of the SMILES profiles averaged for each 1 h local time bin were 43–299 and 6–339 for the mid-latitude region and the equatorial region, respectively. The UARS/MLS observations (Ricaud et al., 2000) were compared with the SMILES observations in Fig. 10. The UARS/MLS ClO data for February at the mid-latitude were averaged over seven years (from 1991 to 1997). Arbitrary offsets were respectively added as 100, 200, 400, 200 and 100 pptv at 0.46, 1,

2.1, 4.6 and 10 hPa to the UARS/MLS ClO observations. The vertical error bars represent $1-\sigma$ standard deviations for both SMILES and UARS/MLS.

The nighttime ClO VMR values are near zero from 00:00–06:00 (a.m.) in the middle stratosphere at 10 hPa (30 km) and 4.6 hPa (35 km). The standard deviations in these time and pressure region present an internal error in the SMILES ClO observations, and not natural variations. The standard deviations are about 20–30 pptv and consistent with the random error of 30 pptv estimated by the error analysis. This indicates that the error analysis results are realistic.

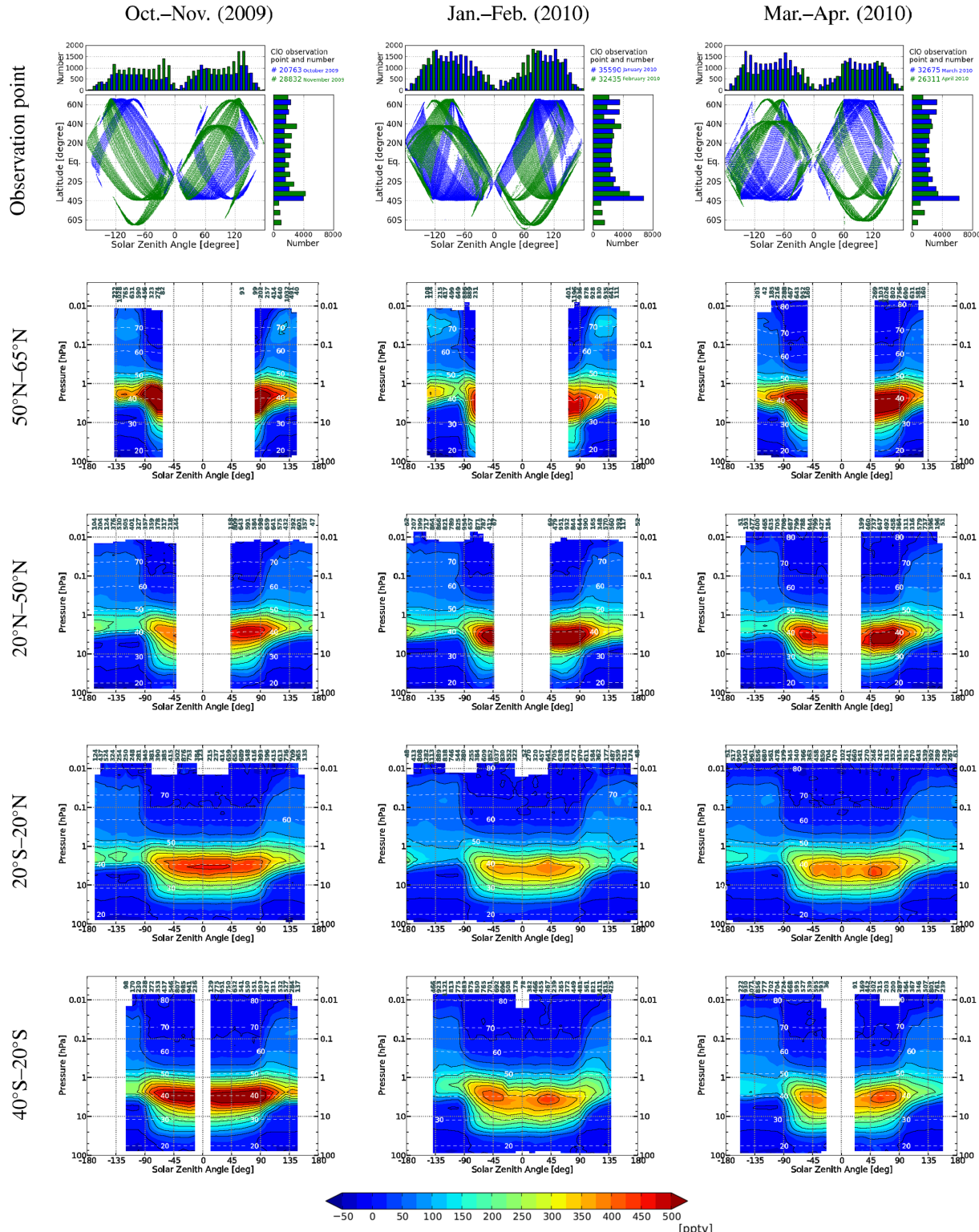


Fig. 11. Seasonal and latitudinal variations in the CIO diurnal variations as a function of SZA and pressure for October–November 2009, January–February 2010 and March–April 2010 and latitudes (50° N– 65° N, 20° N– 50° N, 20° S– 20° N and 40° S– 20° S). The color contour levels are separated by 25 pptv. The altitude is represented by the white dotted line. The numbers of averaged profiles in SZA bins of 10° are indicated at the top of each panel. Only retrieved VMR values that satisfy $\chi^2 < 1$ and $m > 0.8$ are used. The observation points in the top row are represented by dots of different colors for each month. The numbers of scans in an SZA bin of 10° and a latitude bin of 10° are represented by bars at the top and above and to the right. The total number of scans is given at the upper right.

The amplitudes of the observed ClO diurnal variations of 100–300 pptv are significantly larger than the random error of 30 pptv for 100 averaged profiles and the systematic error for SMILES of 10–30 pptv at all pressures.

Moreover, the behaviors of the diurnal variations in the ClO VMR for the stratosphere deduced from the SMILES and the UARS/MLS observations gave a good agreement within their $1-\sigma$ standard deviations as plotted in Fig. 10, although the artificial biases were added to the UARS/MLS data.

4.2 Global ClO diurnal variations

Global diurnal variations of ClO are shown in Fig. 11 as a function of solar zenith angle (SZA) over the SMILES observation period from 12 October 2009 to 21 April 2010 in the stratosphere and the mesosphere for the zonal means of 40° S– 20° S, 20° S– 20° N, 20° N– 50° N and 50° N– 65° N. Note that we define the SZA with a range of -180° to $+180^{\circ}$ in this paper. A negative SZA is used for the a.m. condition and a positive one is for p.m.. There were no SMILES ClO observations in December 2009, because only Bands A and B were used in that month. The contour intervals in Fig. 11 are 25 pptv, which is the total error estimated for an average of 100 profiles. In Fig. 11, each SZA bin of 10° was calculated by averaging more than 100 profiles except for the bins where there were fewer observations because of the orbit of the SMILES observation. The coverage of the SMILES observations was not homogeneous in terms of SZA and location, as indicated by the top panels of Fig. 11.

The ClO VMR in the stratosphere was enhanced during the day and fell to near zero at night. This is consistent with the diurnal variations in ClO VMR observed by UARS/MLS (Fig. 10). The ClO VMR in the afternoon was larger than that in the morning. The lower stratospheric ClO enhancement was strongest in the polar region and faded toward the equatorial region.

It seems that the stratospheric (around 40 km) ClO decreases as a dent near $SZA = 0^{\circ}$; we can most clearly see it in the panel for 40° S– 20° S from January–February. The dent structures are also observed at latitudes and seasons of 40° S– 20° S from March–April, 20° S– 20° N from January–February and March–April, and 20° N– 50° N from March–April. Since there are only a few data near $SZA = 0^{\circ}$ and these are concentrated at specific narrow latitude ranges shown in the top of Fig. 11, further careful analyses are required to understand what the causes of these apparent dent structures are. One possible interpretation of the dent structures could be suggested via a coupling of ClO abundance with the diurnal behavior of atomic O radicals and O₃. The amount of stratospheric ClO is controlled by the following reactions during daytime:



ClO photolysis also occurs but the contribution of this path is much smaller than that of Reaction (R1) and can be ignored. There is a peak amount of O VMR near $SZA = 0^{\circ}$ in the stratosphere (M. Khosravi, personal communication, 2010). The ClO dent structures are produced if [O]/[O₃] $\gg 1$ is satisfied near $SZA = 0^{\circ}$.

The ClO in the mesosphere is enhanced during the night. This feature has been predicted by several models and precisely observed for the first time by SMILES. An event with a higher mesospheric ClO VMR is observed around 70 km in the near-polar region of 50° N– 65° N at nighttime ($SZA = \pm 130^{\circ}$) as shown in Fig. 11. The “ClO mesospheric enhancement” that is located close to the tertiary O₃ maximum (Marsh and Smith, 1995) seems to start from October–November 2009 and fades from March–April 2010. ClO is enhanced through the Reaction (R2) because of the O₃ enhancement. The amplitude of the ClO enhancement is about 100 ppbv. The profile was produced by averaging more than 100 profiles in SZA bins of 10° . This amplitude is three times larger than the estimated total error of 20–30 pptv at 70–80 km and therefore significant.

5 Conclusions

SMILES observed the stratospheric and mesospheric ClO at latitudes between 38° S– 65° N. We quantitatively investigated the errors in the ClO L2r product version 2.1.5 including the errors due to spectrum noise, smoothing, the uncertainties in the radiative transfer calculations and the instrument functions, and the inaccuracies in the spectrum calibrations. The total error for a single-scan observation was less than about 50 pptv at the pressures between 0.1 and 60 hPa. The total error was decreased to 10–30 pptv (about 10%) at the pressures between 0.01 hPa (about 80 km) and 100 hPa (about 16 km) with the averaging of 100–500 profiles. The largest effect on the systematic error was from the air-broadening coefficient, γ_{air} , which contributed up to 8% to the total systematic error of 10% at the pressure of 2 hPa (about 42 km).

We have presented the SMILES global ClO diurnal variations in the stratosphere and the mesosphere. The diurnal variations of the stratospheric ClO showed good agreements with those of UARS/MLS. The behavior of the diurnal variation in ClO was consistent with the known diurnal chemistry. The global diurnal variations of ClO from the stratopause well into the mesosphere, to altitudes of more than 70 km, were obtained for the first time by using the SMILES observations. Nighttime enhancement of ClO at 0.02 hPa (about 70 km) was detected at the high northern latitudes from January–February 2010. The quantitative error analysis provided here indicated that these ClO features were atmospheric in nature.

Acknowledgements. The JEM/SMILES mission is a joint project of the Japan Aerospace Exploration Agency (JAXA) and the National Institute of Information and Communications Technology (NICT). The authors wish to acknowledge the contributions made by M. Shiotani (Kyoto University), M. Suzuki (ISAS/JAXA), and our colleagues at JAXA and NICT for managing and supporting the SMILES mission. The authors also thank K. Muranaga (Systems Engineering Consultants Co., Ltd.) and J. Möller (Molflow Co., Ltd.) for supporting data processing in the Level-2 research product. Further, the authors thank K. Suzuki for providing technical supports. In addition, TOS thanks H. Kanamori and N. Yoshida (Tokyo Institute of Technology) for their kind supports. TOS is supported by a Grant in Aid for Research Fellowship for Young Scientists DC1 (No. 23-9766) from the Japan Society for the Promotion of Science, and the Global COE program “Earth to Earths” of the Ministry of Education, Culture, Sports, Science and Technology, Japan. YK is supported by a Funding Program for Next Generation World-Leading Researchers (NEXT Program) (No. GR101).

Edited by: T. von Clarmann

References

- Baron, P., Ricaud, P., de La Noë, J., Eriksson, J. E. P., Merino, F., Ridal, M., and Murtagh, D. P.: Studies for the Odin sub-millimetre radiometer, II. Retrieval methodology, *Can. J. Phys.*, **80**, 341–356, doi:10.1139/p01-150, 2002.
- Baron, P., Mendrok, J., Kasai, Y., Ochiai, S., Seta, T., Sagi, K., Suzuki, K., Sagawa, H., and Urban, J.: AMATERAU: Model for atmospheric terahertz radiation analysis and simulation, *J. Natl. Inst. Inform. Commun. Technol.*, **55**, 109–121, 2008.
- Baron, P., Urban, J., Sagawa, H., Möller, J., Murtagh, D. P., Mendrok, J., Dupuy, E., Sato, T. O., Ochiai, S., Suzuki, K., Manabe, T., Nishibori, T., Kikuchi, K., Sato, R., Takayanagi, M., Murayama, Y., Shiotani, M., and Kasai, Y.: The Level 2 research product algorithms for the Superconducting Submillimeter-Wave Limb-Emission Sounder (SMILES), *Atmos. Meas. Tech.*, **4**, 2105–2124, doi:10.5194/amt-4-2105-2011, 2011.
- Boissoles, J., Boulet, C., Tipping, R. H., Brown, A., and Ma, Q.: Theoretical calculation of the translation-rotation collision-induced absorption in N₂-N₂, O₂-O₂, and N₂-O₂ pairs, *J. Quant. Spectrosc. Ra.*, **82**, 505–516, doi:10.1016/S0022-4073(03)00174-2, 2003.
- Cazzoli, G. and Puzzarini, C.: Hyperfine structure of the $J=1 \leftarrow 0$ transition of H³⁵Cl and H³⁷Cl: improved ground state parameters, *J. Mol. Spectrosc.*, **226**, 161–168, 2004.
- Drouin, B. J.: Submillimeter measurements of N₂ and air broadening of hypochlorous acid, *J. Quant. Spectrosc. Ra.*, **103**, 558–564, doi:10.1016/j.jqsrt.2006.07.007, 2007.
- Drouin, B. J. and Gamache, R. R.: Temperature dependent air-broadened linewidths of ozone rotational transitions, *J. Mol. Spectrosc.*, **251**, 194–202, doi:10.1016/j.jms.2008.02.016, 2008.
- Hedin, A. E.: Extension of the MSIS thermosphere model into the middle and lower atmosphere, *J. Geophys. Res.*, **96**, 1159–1172, doi:10.1029/90JA02125, 1991.
- Hoshina, H., Seta, T., Iwamoto, T., Hosako, I., Otani, C., and Kasai, Y.: Precise measurement of pressure broadening parameters for water vapor with a terahertz time-domain spectrometer, *J. Quant. Spectrosc. Ra.*, **109**, 2303–2314, doi:10.1016/j.jqsrt.2008.03.005, 2008.
- Kikuchi, K., Nishibori, T., Ochiai, S., Ozeki, H., Irimajiri, Y., Kasai, Y., Koike, M., Manabe, T., Mizukoshi, K., Murayama, Y., Nagahama, T., Sano, T., Sato, R., Seta, M., Takahashi, C., Takayanagi, M., Masuko, H., Inatani, J., Suzuki, M., and Shiotani, M.: Overview and early results of the Superconducting Submillimeter-Wave Limb-Emission Sounder (SMILES), *J. Geophys. Res.-Atmos.*, **115**, D23306, doi:10.1029/2010JD014379, 2010.
- Livesey, N. J., Read, W. G., Froidevaux, L., Waters, J. W., Santee, M. L., Pumphrey, H. C., Wu, D. L., Shippony, Z., and Jarnot, R. F.: The UARS Microwave Limb Sounder version 5 data set: theory, characterization, and validation, *J. Geophys. Res.-Atmos.*, **108**, 4378, doi:10.1029/2002JD002273, 2003.
- Livesey, N. J., Read, W. G., Froidevaux, L., Lambert, A., Manney, G. L., Pumphrey, H. C., Santee, M. L., Schwartz, M. J., Wang, S., Cofield, R. E., Cuddy, D. T., Fuller, R. A., Jarnot, R. F., Jiang, J. H., Knosp, B. W., Stek, P. C., Wagner, P. A., and Wu, D. L.: Version 3.3 Level 2 data quality and description document, Tech. Rep. JPL D-33509, Jet Propulsion Laboratory, available at: <http://mls.jpl.nasa.gov/data/datadocs.php> (last access: 29 June 2012), 2011.
- Manabe, T., Inatani, J., Murk, A., Wylde, R., Seta, M., and Martin, D.: A new configuration of polarization-rotating dual-beam interferometer for space use, *IEEE T. Microw. Theory*, **51**, 1696–1704, doi:10.1109/TMTT.2003.812567, 2003.
- Manabe, T., Nishibori, T., Mizukoshi, K., Otsubo, F., Ochiai, S., and Ohmine, H.: Measurement of the offset-Cassegrain antenna of JEM/SMILES using a near-field phase-retrieval method in the 640 GHz Band, *IEEE T. Antenn. Propag.*, **60**, 3971–3975, doi:10.1109/TAP.2012.2201080, 2012.
- Manney, G. L., Santee, M. L., Rex, M., Livesey, N. J., Pitts, M. C., Veefkind, P., Nash, E. R., Wohltmann, I., Lehmann, R., Froidevaux, L., Poole, L. R., Schoeberl, M. R., Haffner, D. P., Davies, J., Dorokhov, V., Gernandt, H., Johnson, B., Kivi, R., Kyrö, E., Larsen, N., Levelt, P. F., Makshtas, A., McElroy, C. T., Nakajima, H. P. M. C., Tarasick, D. W., Gathen, P., Walker, K. A., and Zinoviev, N. S.: Unprecedented Arctic ozone loss in 2011, *Nature*, **478**, 469–475, doi:10.1038/nature10556, 2011.
- Markov, V. N. and Krupnov, A. F.: Measurements of the pressure shift of the $1_{10}-1_{01}$ water line at 556 GHz produced by mixtures of gases, *J. Mol. Spectrosc.*, **172**, 211–214, 1995.
- Marsh, D. and Smith, A.: The existence of a tertiary ozone maximum in the high-latitude middle mesosphere, *Geophys. Res. Lett.*, **28**, 4531–4534, 2001.
- Masuko, H., Shiotani, M., and SMILES mission team: JEM/SMILES Mission Plan, version 2.1., Tech. Rep. NASDA/CRL, National Space Development Agency of Japan, and Communications Research Laboratory, available at: http://smiles.nict.go.jp/Mission_Plan (last access: 29 June 2012), 2002.

- Mizobuchi, S., Kikuchi, K., Ochiai, S., Nishibori, T., Sano, T., Tamaki, K., and Ozeki, H.: In-orbit measurement of the AOS (Acousto-Optical Spectrometer) response using frequency comb signals, *IEEE J. Sel. Topics Appl. Earth Obs. Remote Sens.*, 5, 977–983 2012.
- Mizoguchi, A., Yagi, T., Kondo, K., Sato, T. O., and Kanamori, H.: Submillimeter-wave measurements of N_2 and O_2 pressure broadening for HO_2 radical generated by Hg-photosensitized reaction, *J. Quant. Spectrosc. Ra.*, 113, 279–285, doi:10.1016/j.jqsrt.2011.11.009, 2012.
- Murtagh, D., Frisk, U., Merino, F., Ridal, M., Jonsson, A., Stegman, J., Witt, G., Eriksson, P., Jiménez, C., Megie, G., de La Noë, J., Ricaud, P., Baron, P., Pardo, J. R., Hauchcorne, A., Llewellyn, E. J., Degenstein, D. A., Gattiner, R. L., Lloyd, N. D., Evans, W. F. J., McDade, I. C., Haley, C. S., Sioris, C., von Savigny, C., Solheim, B. H., McConnell, J. C., Strong, K., Richardson, E. H., Leppelmeier, G. W., Kyrölä, E., Auvinen, H., and Oikarinen, L.: An overview of the Odin atmospheric mission, *Can. J. Phys.*, 80, 309–318, doi:10.1139/p01-157, 2002.
- Ochiai, S., Nishibori, T., Ozeki, H., Kikuchi, K., and Manabe, T.: Superconducting submillimeter-wave limb-emission sounder on the international space station I: radiometric and spectral calibration and data processing, *J. Natl. Inst. Inform. Commun. Technol.*, 55, 83–95, 2008.
- Ochiai, S., Kikuchi, K., Nishibori, T., and Manabe, T.: Gain nonlinearity calibration of submillimeter radiometer for JEM/SMILES, *IEEE J. Sel. Topics Appl. Earth Obs. Remote Sens.* 5, 962–969, 2012a.
- Ochiai, S., Nishibori, T., Kikuchi, K., Mizobuchi, S., Manabe, T., Mitsuda, C., Baron, P., and Ueno, S.: Tangent height accuracy of Superconducting Submillimeter-wave Limb-emission Sounder (SMILES) on International Space Station (ISS), *Proc. IEEE Int. Geosci. Remote Sens. Symp.*, 1290–1293, 2012b.
- Ochiai, S., Kikuchi, K., Nishibori, T., Manabe, T., Ozeki, H., Mizobuchi, S., and Irimajiri, Y.: Receiver performance of Superconducting Submillimeter-Wave Limb-Emission Sounder (SMILES) on the International Space Station, *IEEE Trans. Geosci. Remote Sens.*, doi:10.1109/TGRS.2012.2227758, in press, 2012c.
- Oh, J. and Cohen, E. A.: Pressure broadening of ClO by N_2 and O_2 near 204 and 649 GHz and new frequency measurements between 632 and 725 GHz, *J. Quant. Spectrosc. Ra.*, 52, 151–156, doi:10.1016/0022-4073(94)90004-3, 1994.
- Pardo, J. R., Serabyn, E., and Cernicharo, J.: Submillimeter atmospheric transmission measurements on Mauna Kea during extremely dry El Niño conditions: implications for broadband opacity contributions, *J. Quant. Spectrosc. Ra.*, 68, 419–433, 2001.
- Perrin, A., Puzzarini, C., Colmont, J. M., Verdes, C., Wlodarczak, G., Cazzoli, G., Buehler, S., Flaud, J. M., and Demaison, J.: Molecular line parameters for the “MASTER” (millimeter wave acquisitions for stratosphere/troposphere exchange research) database, *J. Atmos. Chem.*, 51, 161–205, 2005.
- Pickett, H. M., Poynter, R. L., Cohen, E. A., Delitsky, M. L., Pearson, J. C., and Müller, H. S. P.: Submillimeter, millimeter and microwave spectral line catalog, *J. Quant. Spectrosc. Ra.*, 60, 883–890, doi:10.1016/S0022-4073(98)00091-0, 1998.
- Ricaud, P., Chipperfield, M. P., Waters, J. W., Russell III, J. M., and Roche, A. E.: Temporal evolution of chlorine monoxide in the middle stratosphere, *J. Geophys. Res.*, 105, 4459–4470, doi:10.1029/1999JD900095, 2000.
- Rienecker, M. M., Suarez, M. J., Todling, R., Bacmeister, J., Takacs, L., Liu, H.-C., Gu, W., Sienkiewicz, M., Koster, R. D., Gelaro, R., Stajner, I., and Nielsen, J. E.: The GEOS-5 Data Assimilation System – Documentation of Versions 5.0.1, 5.1.0, and 5.2.0, Tech. Rep. NASA/TM-2008-104606, vol. 27, National Aeronautics and Space Administration, available online: <http://mls.jpl.nasa.gov/data/datadocs.php> (last access: 29 June 2012), 2008.
- Rodgers, C. D.: *Inverse Methods for Atmospheric Sounding: Theory and Practice*, Series on Atmospheric, Oceanic and Planetary Physics, vol. 2, World Scientific, Singapore, 3605–3609, 2000.
- Rothman, L. S., Gordon, I. E., Barbe, A., Benner, D. C., Bernath, P. F., Birk, M., Boudon, V., Brown, L. R., Campargue, A., Champion, J.-P., Chance, K., Coudert, L. H., Dana, V., Devi, V. M., Fally, S., Flaud, J.-M., Gamache, R. R., Goldman, A., Jacquemart, D., Kleiner, I., Lacome, N., Lafferty, W. J., Mandin, J.-Y., Massie, S. T., Mikhailenko, S. N., Miller, C. E., Moazzen-Ahmadi, N., Naumenko, O. V., Nikitin, A. V., Orphal, J., Perevalov, V. I., Perrin, A., Predoi-Cross, A., Rinsland, C. P., Rotger, M., Šimečková, M., Smith, M. A. H., Sung, K., Tashkun, S. A., Tennyson, J., Toth, R. A., Vandaele, A. C., and Vander Auwera, J.: The HITRAN 2008 molecular spectroscopic database, *J. Quant. Spectrosc. Ra.*, 110, 533–572, doi:10.1016/j.jqsrt.2009.02.013, 2009.
- Sato, T. O.: Line selection algorithm for atmospheric radiative transfer calculation, *J. Spectrosc. Soc. Jpn.*, 59, 99–101, 2010.
- Sato, T. O., Mizoguchi, A., Mendrok, J., Kanamori, H., and Kasai, Y.: Measurement of the pressure broadening coefficient of the 625 GHz transition of H_2O_2 in the submillimeter-wave region, *J. Quant. Spectrosc. Ra.*, 111, 821–825, doi:10.1016/j.jqsrt.2009.11.022, 2010.
- Schreier, F. and Kohlert, D.: Optimized implementations of rational approximations – a case study on the Voigt and complex error function, *Comput. Phys. Commun.*, 179, 457–465, doi:10.1016/j.cpc.2008.04.012, 2008.
- Schwartz, M. J., Lambert, A., Manney, G. L., Read, W. G., Livesey, N. J., Froidevaux, L., Ao, C. O., Bernath, P. F., Boone, C. D., Cofield, R. E., Daffer, W. H., Drouin, B. J., Fetzer, E. J., Fuller, R. A., Jarnot, R. F., Jiang, J. H., Jiang, Y. B., Knosp, B. W., Krüger, K., Li, J.-L. F., Mlynczak, M. G., Pawson, S., Russell, J. M., Santee, M. L., Snyder, W. V., Stek, P. C., Thurstans, R. P., Tompkins, A. M., Wagner, P. A., Walker, K. A., Waters, J. W., and Wu, D. L.: Validation of the aura microwave limb sounder temperature and geopotential height measurements, *J. Geophys. Res.-Atmos.*, 113, D15S11, doi:10.1029/2007JD008783, 2008.
- Urban, J., Baron, P., Lautié, N., Schneider, N., Dassas, K., Ricaud, P., and de La Noë, J.: Molire (v5): a versatile forward-and inversion model for the millimeter and sub-millimeter wavelength range, *J. Quant. Spectrosc. Ra.*, 83, 529–554, doi:10.1016/S0022-4073(03)00104-3, 2004.

- Urban, J., Murtagh, D., Lautié, N., Barret, B., Dupuy, É., de La Noë, J., Eriksson, P., Frisk, U., Jones, A., Le Flochmoën, É., Olberg, M., Piccolo, C., Ricaud, P., and Rösevall, J.: Odin/SMR Limb Observations of Trace Gases in the Polar Lower Stratosphere during 2004–2005, in: Atmospheric Science Conference, vol. 628 of ESA Special Publication, Frascati, Italy, 2006.
- van Vleck, J. H. and Weisskopf, V. F.: On the shape of collision-broadened lines, *Rev. Mod. Phys.*, 17, 227–236, doi:10.1103/RevModPhys.17.227, 1945.
- Waters, J. W., Froidevaux, L., Read, W. G., Manney, G. L., Elson, L. S., Flower, D. A., Jarnot, R. F., and Harwood, R. S.: Stratospheric ClO and ozone from the microwave limb sounder on the upper atmosphere research satellite, *Nature*, 362, 597–602, doi:10.1038/362597a0, 1993.
- Waters, J. W., Froidevaux, L., Harwood, R. S., Jarnot, R. F., Pickett, H. M., Read, W. G., Siegel, P. H., Cofield, R. E., Filipiak, M. J., Flower, D. A., Holden, J. R., Lau, G. K., Livesey, N. J., Manney, G. L., Pumphrey, H. C., Santee, M. L., Wu, D. L., Cuddy, D. T., Lay, R. R., Loo, M. S., Perun, V. S., Schwartz, M. J., Stek, P. C., Thurstans, R. P., Boyles, M. A., Chandra, K. M., Chavez, M. C., Chen, G.-S., Chudasama, B. V., Dodge, R., Fuller, R. A., Girard, M. A., Jiang, J. H., Jiang, Y., Knosp, B. W., Labelle, R. C., Lam, J. C., Lee, A. K., Miller, D., Oswald, J. E., Patel, N. C., Pukala, D. M., Quintero, O., Scaff, D. M., Vansnyder, W., Tope, M. C., Wagner, P. A., and Walch, M. J.: The Earth Observing System Microwave Limb Sounder (EOS MLS) on the aura satellite, *IEEE T. Geosci. Remote*, 44, 1075–1092, doi:10.1109/TGRS.2006.873771, 2006.